Non-proteinaceous complexes III and IV mimicking electron transfer in the mitochondrial respiratory chain

Iago A. Modenez[1], Lucyano J. A. Macedo[1], Antonio F. A. A. Melo[2], Andressa R. Pereira[4], Osvaldo N. Oliveira, Jr.[4], Frank N. Crespilho[1*].

[1]São Carlos Institute of Chemistry, University of São Paulo, São Carlos 13560-970, São Paulo, Brazil.

[2]Federal Institute of Education, Science and Technology of Piauí, Teresina 64000-040, Piauí, Brazil.

[4]São Carlos Institute of Physics, University of São Paulo, São Carlos 13560-590, São Paulo, Brazil.

*Correspondence to: frankcrespilho@iqsc.usp.br

ABSTRACT

Synthetic biology pursues the understanding of biological processes and their possible mimicry with artificial bioinspired materials. We explore the redox properties of magnetic iron oxide nanoparticles to mimic the redox activity of complexes III and IV towards cytochrome c. We demonstrate that these nanoparticles, incorporated as non-proteinaceous complexes III and IV in a mitochondrial cell membrane model, catalyze electron transfer similarly to natural complexes. The associated molecular mechanism was experimentally proven in solution and in a Langmuir-Blodgett film; the protein-nanoparticle interactions are governed mainly by electrostatic forces, followed by electron transfer between the iron sites of the nanoparticles and the heme group. This work presents the first experimental demonstration that inorganic nanostructured systems may behave as proteins in the cell membrane.

Keywords: Biomimetic material, Cytochrome c, Iron oxides nanoparticles, Direct electron transfer, Mitochondrial cell membrane model.

INTRODUCTION

Processes involving electron transfer (ET) reactions are essential for living organisms' cellular respiration and energy acquisition (*1*). The mitochondrial respiratory chain in eukaryotic cells is one significant example of biological ET, which consists of a series of electron-carrying membrane-embedded proteins whose electron transport is facilitated by a small soluble redox protein, referred to as cytochrome c (Cyt c) (*2*). Cytochromes, in general, play crucial roles in ET associated with energy metabolisms and in apoptosis (*3*). In the mitochondrial respiratory chain, the electron received by Cyt c from complex III derives from ubiquinol, and it is later transferred from Cyt c to complex IV, which eventually catalyzes the complete reduction of molecular oxygen to water. The interaction of Cyt c with these complexes is governed by long-range electrostatic interactions in addition to specific non-polar forces surrounding the heme crevice(*4*).

The design of biomimetic materials has triggered research in synthetic biology (*5,6*), with molecules such as proteins, lipids, and DNA, associated with artificial components, used to mimic life processes and design biological systems nonexistent in nature (*7*). Iron oxides are promising inorganic materials for synthetic biology due to their abundance and ubiquity in the environment as a redox mediator in microbial cellular metabolism (*8*,*9*). Electron exchange usually occurs across the cell membrane and iron-based oxides interface, promoted by cellular heme-containing c-types cytochrome proteins (*10–12*).

Magnetite (Fe_3O_4-NPs) and maghemite (γ-Fe_2O_3-NPs) are iron oxides differing only by Fe^{2+} cationic vacancies in their unit cells, i.e., Fe_3O_4-NPs contain Fe^{2+} and Fe^{3+} in a 1:2 stoichiometric ratio, while γ-Fe_2O_3-NPs contain only Fe^{3+}. These nanoparticles have been used in biomedical and technological applications; for instance, Fe_3O_4-NPs may be classified as *nanozymes* due to their intrinsic peroxidase-like activity, catalyzing oxidation reactions similarly to active iron sites within the heme group of enzymes (*12*). Since ET reactions involving Fe_3O_4-NPs/γ-Fe_2O_3-NPs and proteins have been reported (*14*), we hypothesize that these materials are able to mimic the activity of complexes III and IV towards Cyt c. Herein, we show a bioinspired system of one catalytic step in the mitochondrial respiratory chain based on the direct ET between iron oxides nanoparticles and Cyt c, as depicted in Fig. 1. Additionally, we elucidate the nanoparticle-protein ET mechanism at a molecular scale and provide the basis for the development of a novel class of biomimetic model materials.

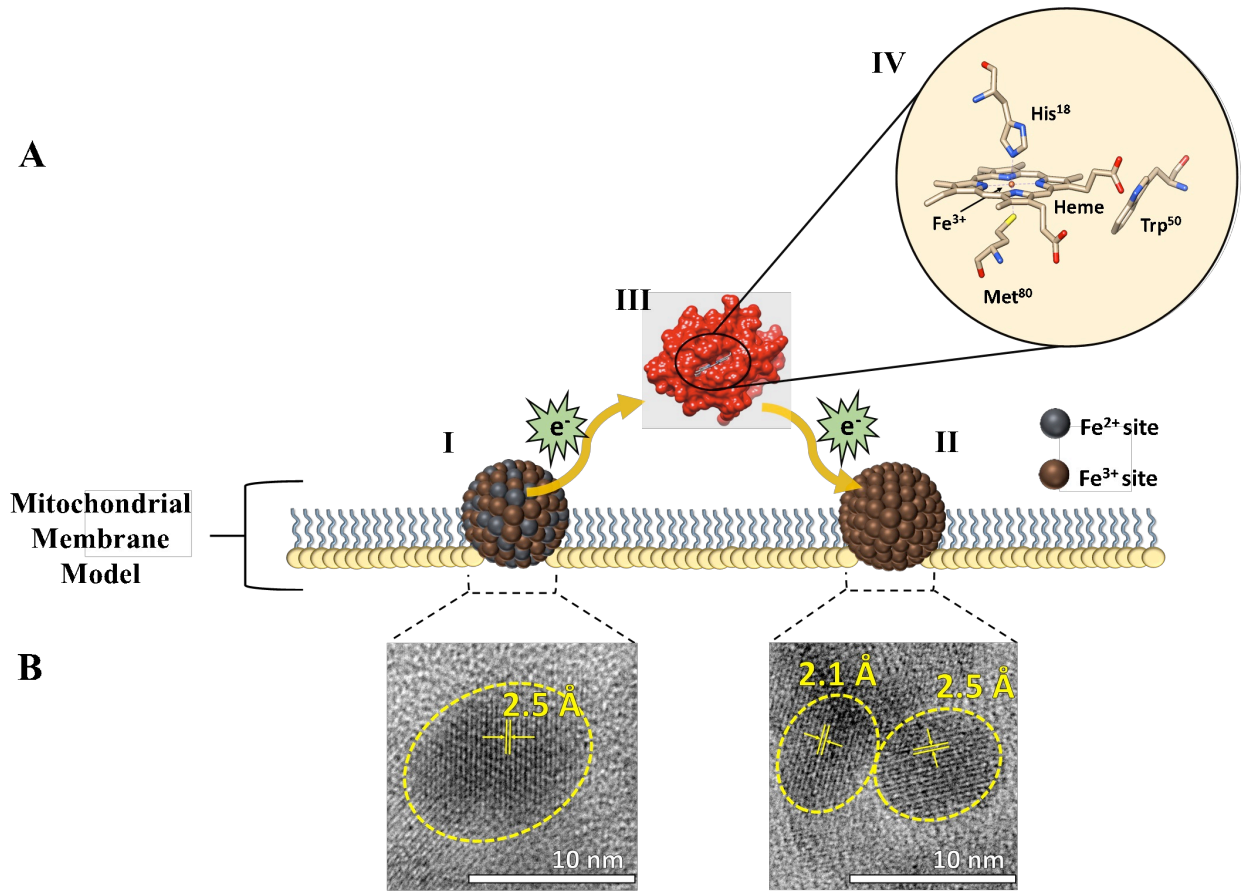

Fig. 1. Representation of the biomimetic membrane model. (A) Fe_3O_4-NPs (**I**) and γ-Fe_2O_3-NPs (**II**) incorporated in a monolayer mitochondrial cell membrane model. The Cyt c protein (**III**) – not incorporated in the membrane – has a heme group (**IV**) in which the iron changes between Fe^{3+} and Fe^{2+} in redox reactions; (**B**) TEM images indicate crystalline Fe_3O_4-NPs and γ-Fe_2O_3-NPs with average sizes of 10 ± 3 nm and 11 ± 3 nm, respectively. The 2.5 Å and 2.1 Å lattice fringes shown in the TEM images correspond to the (311) and (400) planes of the crystalline structure, respectively.

MATERIALS AND METHODS

Materials

The materials used were ferric chloride hexahydrate ($FeCl_3.6H_2O$, Sigma-Aldrich, 99%), ferrous chloride tetrahydrate ($FeCl_2.4H_2O$, Sigma-Aldrich, 99%), hydrochloric acid (HCl, Sigma-Aldrich, 37%), sodium hydroxide (NaOH, Synth, 98%), bovine heart cytochrome c (Sigma-Aldrich, purity ≥ 95%, CAS Number: 9007-43-6), Sephadex® G-75 superfine (Sigma-Aldrich), sodium phosphate dibasic (Na_2HPO_4, Synth, 98%), potassium dihydrogen phosphate (KH_2PO_4, Synth, 98%),

potassium chloride (KCl, Synth, 99%), sodium chloride (NaCl, Synth, 99%), nitric acid (HNO_3, Vetec, 65%), ferric nitrate ($Fe(NO_3)_3$), Sigma-Aldrich, 98%), epoxy resin (Brascola), 1,1',2,2'-tetramyristoyl cardiolipin (CL, Avanti Polar Lipids, 99%), 1,2-dipalmitoyl-sn-glycero-3-phosphoethanolamine (DPPE, Avanti Polar Lipids, 99%), 1,2-dipalmitoyl-sn-glycero-3-phosphocholine (DPPC, Sigma-Aldrich, 99%), HPLC-grade chloroform ($CHCl_3$, Panreac, 99.9%). The solutions were prepared using ultrapure water provided by a Milli-Q system from Millipore (resistivity 18.2 MΩ cm).

Fe_3O_4 nanoparticles synthesis and characterization

Magnetite nanoparticles (Fe_3O_4-NPs) were synthesized by co-precipitation as reported in the literature (*15*). To do so, $FeCl_3.6H_2O$ (5.4 g) and $FeCl_2.4H_2O$ (2.0 g) were dissolved in a deaerated 10 mmol L^{-1} HCl solution (25 mL). Under a N_2 saturated atmosphere, a deaerated 1.5 mol L^{-1} NaOH solution (250 mL) was added dropwise to the Fe^{3+}/Fe^{2+} mixture with vigorous stirring at 80 ºC to generate the magnetite nanoparticles (Equation 1). After approximately 30 min under stirring, the nanoparticles in suspension were separated with a magnet and continuously washed with deionized water until neutral pH. Finally, a stock suspension (5 mg mL^{-1}) was prepared dispersing the Fe_3O_4-NPs in a 5 mmol L^{-1} phosphate buffer saline (PBS) buffer (pH 7.4).

$$2\ Fe^{3+}_{(aq)} + Fe^{2+}_{(aq)} + 8\ OH^-_{(aq)} \longrightarrow Fe_3O_{4(s)} + 4\ H_2O_{(l)} \qquad \text{(Equation 1)}$$

Transmission electron microscopy (TEM) images were acquired using a JEOL JEM-2100 operating at 200 kV. The sample was prepared dropping a diluted nanoparticle suspension on a 400-mesh cupper grid coated with lacey carbon film and then drying it under vacuum. The average size and polydispersity were determined using ImageJ software based on a count of 150 nanoparticles. X-ray powder diffraction pattern (XRD) data were obtained using a Bruker D8 Advanced diffractometer with Cu K_α (λ = 1.5406 Å) radiation. The scanning angle varied between $25^o < 2\theta < 100^o$ with a scanning rate of 0.02º each 10 s. The average particle diameter was calculated based on the three most intense peaks (311), (511) and (440) using Scherrer's equation ($D = K\lambda/(B \cos \theta)$), where K is the crystalline-shape factor (ca. 0.9 for spherical particles), λ is the wavelength of the X-ray radiation, B is the full-width at half-maximum of the X-ray diffraction peak and θ is the Bragg angle (*16*). The Fourier-transform infrared (FTIR) spectra were recorded

in a Bruker Vertex 70v spectrometer using the transmission mode (1 mg of lyophilized protein and 99 mg of KBr) in the region of 4000-450 cm^{-1}. Each spectrum was obtained by averaging 32 interferograms at a 4 cm^{-1} resolution using DLaTGS (Deuterated Lanthanum L-alanine doped Triglycine Sulphate) detector. The Zeta potential (ζ) and Dynamic Light Scattering (DLS) measurements were performed on a Zetasizer Nano Series Malvern instrument at 25 ºC. A Fe_3O_4-NPs suspension was prepared (0.1 mg mL^{-1}) in PBS buffer 5 mmol L^{-1} (pH 7.4) and, then, filtered using 0.2 μm pore sized membranes in order to remove any impurity before the measurements. The reported data were averaged over 3 accumulations.

Cytochrome c structural characterization

Cytochrome c was chromatographically purified using a Sephadex G-75 superfine matrix with PBS buffer 5 mmol L^{-1} (pH 7.4) as eluent. All protein solutions were prepared in PBS buffer 5 mmol L^{-1} (pH 7.4). Spectroscopy measurements in ultraviolet/visible region (UV-vis) were performed using a spectrophotometer Jasco V-760 between 200 and 700 nm with a quartz microcuvette (1.0 cm optical path length). The cytochrome c solution was prepared in a concentration of 81 μmol L^{-1}. Circular Dichroism (CD) spectra were recorded on a Jasco J-815 spectropolarimeter in the range of 210 to 500 nm with an averaged data over 10 accumulations at 25 ºC using a cell of 1.0 cm optical path length. The sample solutions were prepared in a concentration of 10 μmol L^{-1} and the spectra were deconvoluted using CDNN software. FTIR spectra were recorded in a Bruker Vertex 70v spectrophotometer in the attenuated total reflectance (ATR) mode equipped with a single-bounce diamond crystal and a DLaTGS (Deuterated Lanthanum L-alanine doped Triglycine Sulphate) detector. The sample was dropped (10 μL of an 81 μmol L^{-1} cytochrome c solution) and dried on the crystal and the spectra were recorded in the region 3800-380 cm^{-1} at a resolution of 4 cm^{-1} with an average data over 32 accumulations for each spectrum. The amide I region (1700-1600 cm^{-1}) was deconvoluted using the second order derivative and the main bands were assigned according to the literature (*17*): 1658-1650 cm^{-1} (α-helix), 1642-1624 cm^{-1} (β-sheet) and 1690-1666 cm^{-1} (β-turn). Zeta potential (ζ) and DLS measurements were performed in the same conditions as described in the previous section. Both Fe_3O_4-NPs and cytochrome c suspensions were prepared in a concentration of 0.1 mg mL^{-1} and mixed in a 1:1 proportion for the Fe_3O_4-NPs-Cyt c system analysis. The cyt c residual charge was calculated using ProtParam software from an amino acids sequence analysis.

Adsorption measurements

The adsorption measurements were carried out to determine the equilibrium distribution of cyt c in solution and on nanoparticles, which was done by taking the decrease in UV-vis absorption of the protein. Since the contact between Fe_3O_4-NPs and oxidized cytochrome c (ferricytochrome c) leads to reduction of the protein and then to a different absorption spectrum, its concentration in solution was probed using the aromatic band at 280 nm. We assume that reduction does not cause significant change in conformation or arrangement of the polypeptide chain (*18*). The measurements were carried out in a spectrophotometer Jasco V-760 from 200 to 700 nm, with a quartz microcuvette (1.0 cm optical path length), using a fixed concentration of cyt c (10 μmol L^{-1} in PBS buffer 5 mmol L^{-1} pH 7.4) and Fe_3O_4-NPs (432 μmol L^{-1}). The mixture was continuously shaken, and the decrease in protein concentration was monitored through time.

Steady-state fluorescence measurements

The data were collected in a Hitachi F-4500 spectrofluorimeter with a 1.0 cm optical path length at three temperatures (15, 25 and 35 ºC). The excitation and emission slits were set at 5.0 nm and the spectra were recorded in a wavelength range of 330-370 nm with a scanning rate of 240 nm min^{-1}. Fluorescence emission was measured upon exciting a 40 μmol L^{-1} cytochrome c solution at 300 nm in the presence of various Fe_3O_4 nanoparticles concentrations (216, 259, 345, 432, 864 and 1296 μmol L^{-1}). The reference spectra were taken solely with PBS buffer and Fe_3O_4-NPs, since the nanoparticles do not absorb light at the wavelength region under study. Their effect in the fluorescence analysis is negligible. The quenching mechanism was determined using Stern-Volmer equation (*19*) (Equation 2).

$$F_0 / F = 1 + K_{sv}\, cQ \qquad \text{(Equation 2)}$$

where F_0 and F are the fluorescence intensities of the protein in the absence and presence of the quencher Q, respectively, K_{sv} is the Stern-Volmer quenching constant and cQ is the quencher concentration. The bimolecular quenching constant (K_q) was calculated from Equation 3.

$$K_{sv} = K_q\, \tau_0 \qquad \text{(Equation 3)}$$

where τ_0 is the average bimolecular fluorescence lifetime in the absence of the quencher, taken as 10^{-8} s (*20,21*). The number of binding sites per protein molecule (n) and the binding constant (K_b) were calculated using Equation 4 (*19*).

$$\log ((F_0 - F)/F) = \log K_b + n \log cQ \qquad \text{(Equation 4)}$$

Kinetic and Thermodynamic parameters

The ferricytochrome c reduction by Fe_3O_4-NPs was studied using *in situ* UV-visible absorption spectroscopy. All the protein solutions were prepared in PBS buffer 5 mmol L^{-1} (pH 7.4). The data were collected using a spectrophotometer Jasco V-760 with a quartz microcuvette (1.0 cm optical path length). In order to determine the kinetic parameters, the reactions were carried out in a pseudo-first order regime, where the Fe_3O_4-NPs were in excess compared with ferricytochrome c. The parameters were evaluated by fixing the ferricytochrome c solution concentration (10 µmol L^{-1}) and varying the nanoparticles concentration (108, 216, 432, and 864 µmol L^{-1}) at four temperatures (25, 30, 35 and 40 ºC). The equipment was set to perform absorbance (A) measurements each 10 s at a fixed wavelength (550 nm), corresponding to the formation of reduced cyt c. Owing to the excess of Fe_3O_4-NPs, it is possible to assume that their concentration is constant throughout the reaction. So, one can obtain the apparent pseudo-first order rate constant (k_{obs}) as follows (*22*) (Equation 5):

$$v = k_{obs} [Cyt\ c] \qquad \text{(Equation 5)}$$

where v is the reaction rate and [*Cyt c*] is the concentration of ferricytochrome c solution. k_{obs} may be obtained by plotting ln (A_∞ - A) *versus* time (t), which should result in a straight line with slope k_{obs}. The second-order rate constant (k) may be obtained correlating k_{obs} with the Fe_3O_4-NPs concentration (*22*) (Equation 6), since:

$$k_{obs} = k [Fe_3O_4\text{-NPs}] \qquad \text{(Equation 6)}$$

where [Fe_3O_4-NPs] is the concentration of Fe_3O_4 nanoparticles. The experiments were carried out in the dark and both in opened and inert atmosphere to eliminate any doubt about the influence of atmospheric oxygen.

The activation energy was calculated using the Arrhenius equation (*23*) (Equation 7), since plotting ln k against $1/T$ gives a straight line with a slope of $-E_a/R$. Activation parameters based on the transition state theory, such as $\Delta H^{\ddagger}$ and $\Delta S^{\ddagger}$, were calculated though the Eyring plot (Equation 8) relating ln (k/T) with $1/T$, where the slope corresponds to $-\Delta H^{\ddagger}/R$ and the y-intercept corresponds to ln $(k'/h) + \Delta S^{\ddagger}/R$, where k' is the Boltzmann constant and h is the Planck constant (*22*).

$$k = Ae^{(-Ea/RT)} \qquad \text{(Equation 7)}$$

$$\ln (k/T) = -\Delta H^{\ddagger}/RT + \ln (k'/h) + \Delta S^{\ddagger}/R \qquad \text{(Equation 8)}$$

The thermodynamic parameters of interaction between cyt c and Fe_3O_4-NPs were investigated using the van't Hoff equation (*24*) (Equation 9), from which ΔH° and ΔS° are obtained. $\Delta G^{\circ}_{binding}$ is calculated using the Gibbs-Helmholtz equation (Equation 10).

$$\ln K_b = -\Delta H^{\circ}/RT + \Delta S^{\circ}/R \qquad \text{(Equation 9)}$$

$$\Delta G^{\circ} = \Delta H^{\circ} - T\Delta S^{\circ} \qquad \text{(Equation 10)}$$

γ-Fe_2O_3 nanoparticles synthesis and characterization

The maghemite nanoparticles (γ-Fe_2O_3-NPs) were synthesized with method reported in (*25*). An aliquot of 10 mL of a suspension of Fe_3O_4 nanoparticles was stirred for 10 min in a 4 mol L^{-1} nitric acid solution. The precipitate was magnetically separated, washed several times with deionized water, and mixed with a 0.1 mol L^{-1} ferric nitrate solution at 90 ºC for 30 min (Equation 11). The brown precipitate (maghemite) was separated from the solution and washed several times with deionized water. Finally, a stock suspension of 5 mg mL^{-1} was prepared dispersing the γ-Fe_2O_3-NPs in a 5 mmol L^{-1} PBS buffer (pH 7.4).

$$2\ Fe_3O_{4(s)} + HNO_{3(aq)} \longrightarrow \gamma\text{-}3\ Fe_2O_{3(s)} + HNO_{2(aq)} \qquad \text{(Equation 11)}$$

Transmission electron microscopy (TEM) images were acquired using a JEOL JEM-2100 operating at 200 kV. The sample was prepared dropping a diluted suspension of nanoparticles on a 400 mesh cupper grid coated with lacey carbon film and then drying it under vacuum. The average size and polydispersity were determined using ImageJ software from 100 nanoparticles. X-ray powder diffraction pattern (XRD) data were obtained using a Bruker D8 Advanced diffractometer with Cu K_α (λ = 1.5406 Å) radiation. The scanning angle varied between $25^o < 2\theta < 100^o$ with a scanning rate of 0.02º each 10 s. The average particle diameter was calculated based on the three most intense peaks (311), (511) and (440) using Scherrer's equation.

Langmuir monolayers and Langmuir-Blodgett (LB) films

The lipid solutions were used without further purification. Surface pressure measurements were performed with a Mini KSV Langmuir trough with a Wilhelmy plate made of filter paper as the pressure (π) sensor. The spreading solutions were prepared by dissolving DPPC in chloroform, and CL and DPPE in a mixture of methanol and chloroform. First, we prepared one solution of 1.0 mg mL^{-1} for each compound, and then the ternary lipid mixture was obtained by mixing appropriate volumes of respective stock solution, using a molar fraction of 0.50:0.30:0.20 (DPPC:DPPE:CL), which corresponds to the composition of the mitochondrial membrane, referred to as DPPC-DPPE-CL. The aqueous subphase consisted of PBS buffer (pH 7.4) prepared in ultrapure water in absence and in the presence of a mixture of either Fe_3O_4 or γ-Fe_2O_3 nanoparticles. The lipid mixture dissolved in chloroform or in the mixture of methanol/chloroform was spread over the subphase surface with a Hamilton microsyringe. The time for solvent evaporation and the interaction between the lipids and the nanoparticles were 10 min, and the monolayers were compressed with two symmetric moving barriers at a compression rate of 10 cm^2 min^{-1}. The surface-pressure measurements were carried out at 22±1 ºC and repeated at least three times to ensure reproducibility. All experiments were performed in a class 10000 clean room. The Brewster angle microscopy (BAM) images for the Langmuir monolayers were acquired with an EP4 imaging ellipsometer from Accurion using an Ultraobjective at angles of incidence and view 53.1º, polarization at 2º, and analyzer at 10º. The images were geometrically corrected using the Data Studio software from Accurion. The equipment is coupled with a KSV trough, and therefore the images were taken while the Langmuir monolayers were being formed.

The transfer of DPPC-DPPE-CL and DPPC-DPPE-CL-nanoparticles monolayers onto solid supports in the form of Langmuir-Blodgett (LB) films was performed at a constant surface pressure of 30 mN m^{-1}, a temperature equals to 22 ± 1 ºC, and a deposition rate of 10 mm min^{-1}. The supports used were glass (for the *in situ* UV-vis measurements) and ITO (for the electrochemical measurements). In all cases, a one-layer Y-type LB film was deposited with control of the transfer ratio during the upstroke. The LB film was allowed to dry for 30 min., and then stored at 4 ºC for later measurements. Polarization-modulation infrared reflection absorption spectroscopy (PM-IRRAS) was performed in the LB films using KSV PMI 550 instrument. In PM-IRRAS, an incoming light is modulated at high frequency between *s*- and *p*-polarization, thus permitting the simultaneous measurement of the polarized reflectivities for the parallel and perpendicular directions to the plane of incidence. The experiments were performed at an incident angle of 81º, and an average of 9000 scans were collected for each spectrum at resolution of 8 cm^{-1}. The PM-IRRAS spectrum of an ITO surface was used as background. Measurements were carried out in a class 10000 clean room at 22±1 ºC.

Electrochemical measurements

The data were collected in an Autolab PGSTAT204 potentiostat/galvanostat (Metrohm). The experiments were performed using an electrochemical cell with three electrodes comprising of platinum plate as auxiliary electrode, a saturated $Ag/AgCl_{sat}$ as the reference electrode, and as working electrode we used three ITO-based electrodes (indium tin oxide): one with only one-layer LB film (which will be referred to as LB film), another with a ferricytochrome c film on top of the one-layer LB film (referred to as LB film + Cyt c), and the third one with a ferricytochrome c film on top of the one-layer LB film with the incorporated nanoparticles (referred to as LB + NPs film + Cyt c). PBS buffer 0.1 mol L^{-1} (pH 7.4) was used as supporting electrolyte. Argon was purged for at least 30 min prior to recording the voltammograms at 25 ºC in a potential window from 0.4 V to -0.2 V (*vs* $Ag/AgCl_{sat}$) at a 5 mV s^{-1} scan rate for ten cycles. The current in all electrochemical measurements was normalized by the geometric electrode area, resulting in a current density value (*j*).

In situ optical absorption spectroscopy

The data were collected in an AvaSpec-2048 (an Avantes spectrophotometer with Avalight-DHS deuterium-halogen light sources) using an optical-fiber module. The experiments were conducted in the dark with the set up shown in Figure 5c. First, a small region of the membrane on the glass was isolated using epoxy resin; after complete drying, 100 µL of a concentrated ferricytochrome c solution (810 µmol L^{-1} in PBS buffer 5 mmol L^{-1} pH 7.4) were dropped on the isolated region. *In situ* absorption measurements were carried out at 25 ºC in the range between 350 and 600 nm, with a spectrum taken every 20 s during 30 min. The data were averaged over 200 accumulations at an integration time of 20 ms.

RESULTS AND DISCUSSION

Fe_3O_4-NPs as a biomimetic complex III

Bare Fe_3O_4-NPs were synthesized via co-precipitation (*26*, *27*) (Fig. S1, S2). In the presence of oxidized Cyt c, ET from Fe_3O_4-NPs to the protein occurs spontaneously, leading to a reduction of the heme group. The UV-vis absorption spectra of oxidized and reduced Cyt c states – also known as ferricytochrome c (ferricyt c) and ferrouscytochrome c (ferrouscyt c), respectively – in Fig. 2A, B feature typical protein absorption bands in the UV region (*28*). For hemeproteins such as Cyt c these include a band at 409 nm (Soret band), a shoulder at 356 nm, and a weak band at 530 nm (Q band) due to the protein porphyrin chromophore. Shifts in Soret and Q bands are related to changes in the oxidation state of the iron ion in the heme group. Therefore, these differences in the spectroscopic signatures of Cyt c are useful for probing protein reduction. After the addition of Fe_3O_4-NPs to the ferricytochrome c solution, the Soret band and the shoulder shifted to 415 nm and 315 nm, respectively, while the band at 530 nm split into two well-defined bands at 520 nm and 550 nm (Fig. 2A, B, red). These spectroscopic changes may also be associated with conformational rearrangements in the heme microenvironment (*29*) with the iron modified from hexacoordinated in ferricytochrome c to pentacoordinated in ferrouscytochrome c due to the rupture of the Fe-S(Met) bond (Fig. 2C).

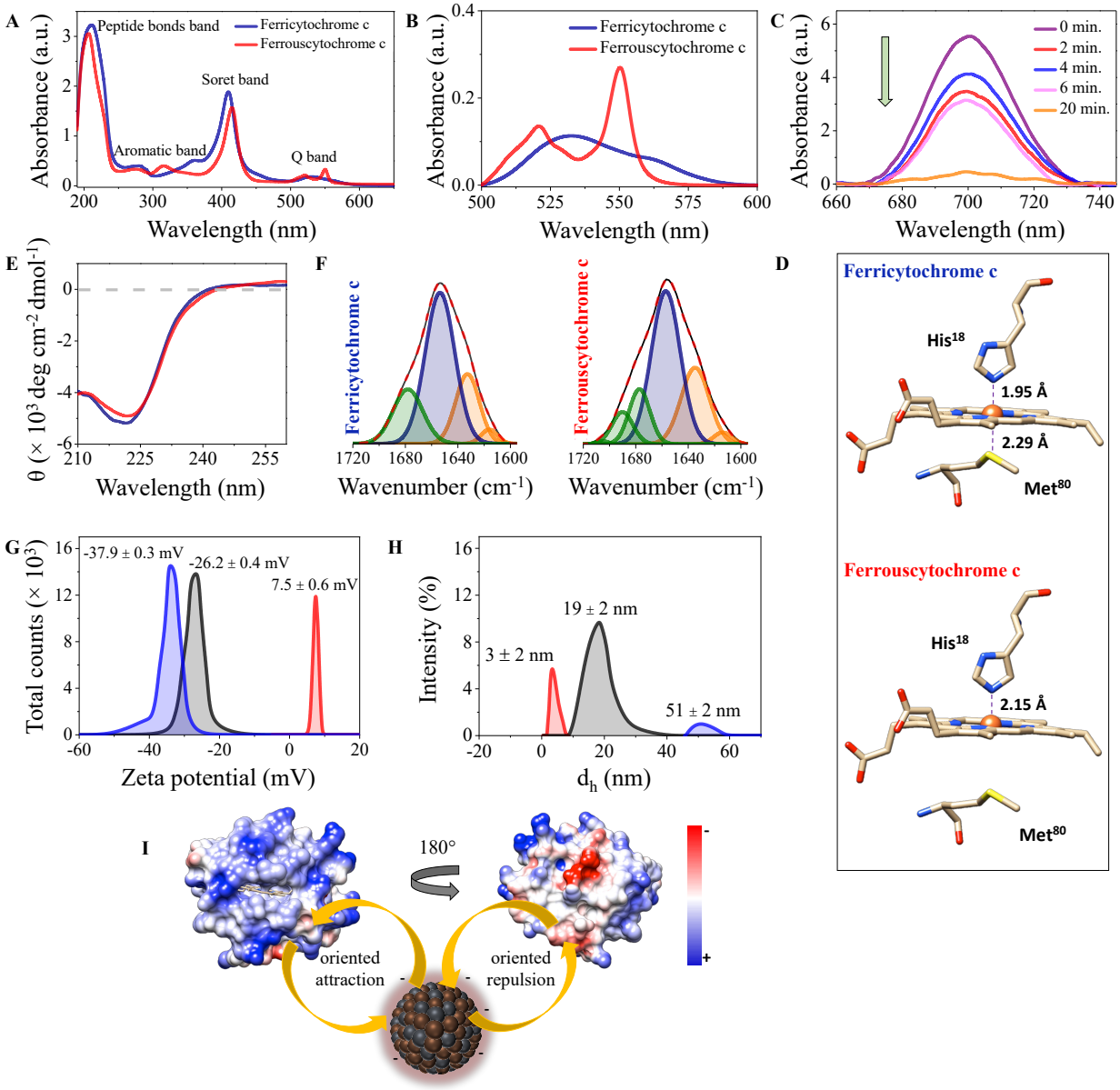

Fig. 2. Fe_3O_4-NPs and ferricytochrome c ET. (**A**) UV-vis spectra for ferricytochrome c (●) and its reduction by bare Fe_3O_4-NPs (●); (**B**) An expanded scale of the Q band region; (**C**) UV-vis spectra showing the decrease in the charge-transfer absorption band due to the Fe-S(Met) bond rupture through the heme group reduction at 0 min (●), 2 min (●), 4 min (●), 6 min (●), and 20 min (●); (**D**) Schematic representation of the heme group in ferricytochrome c and ferrouscytochrome c; (**E**) VCD spectra of ferricytochrome c (●) and ferrouscytochrome c (●); (**F**) Deconvoluted amide I region for ferri and ferrouscytochrome c, respectively, obtained using FTIR spectroscopy. Each color indicates a different type of secondary structure, *viz.*: α-helix (●), β-sheet (●), and others (major contribution of β-turn structure) (●); (**G**) Zeta potential for Fe_3O_4-NPs (●), Fe_3O_4-NPs-Cyt c system (●), and ferricyt c (●); (**H**) DLS of nonadsorbed Cyt c (●), Fe_3O_4-NPs (●), and Fe_3O_4-NPs-Cyt c system (●); (**I**) Front and back Cyt c electrostatic potential map showing an oriented attraction between the heme group and the NP surface, while there is an oriented repulsion between the latter and the protein back side.

After approximately 20 min, just a small amount of Cyt c remained oxidized. This bond rupture leads to some extent of conformational changes surrounding the heme group, such as an increase in the Fe-N(His) bond length and the Met residue displacement responsible for an opening of the heme crevice (*30*) (Fig. 2D). Reported heterogeneous ET (*31*) involving a decaheme c-type cytochrome and $Fe_{3-x}Ti_xO_4$-NPs suggests that the protein accesses the nanoparticles' superficial Fe^{2+}, which would hint some initial mechanistic insights of Fe_3O_4-NPs-ferricyt c interaction, as the ones shown in Fig. 2I and 3.

According to the vibrational UV circular dichroism (VCD) and infrared absorption (FTIR) measurements, protein reduction occurs without considerable changes in its secondary structure. The VCD spectrum shows a typical α-helical band at 222 nm (*32*), which is slightly decreased when Cyt c is reduced (Fig. 2E, red). The spectra deconvolution shows a 4% decrease in the α-helical content after protein reduction, which is a negligible loss of secondary content (see Table S1). In addition, although there is no indication of changes in the tertiary structure; the shift in the Soret band maximum points to an iron reduction in the heme moiety (Fig. S3). These results were corroborated by FTIR data in Fig. 2F. Table S1 brings the percentage of each secondary structure determined by deconvolution of the amide I band in the FTIR spectrum, where the reduction in α-helical content is only 5% between ferri and ferrouscytochrome c. Therefore, one may infer that Fe_3O_4-NPs can behave as a biomimetic material of the complex III from the mitochondrial respiratory chain.

Nanoparticle (NP)-protein interactions mediated by electrostatic and non-polar forces

In order to describe the NP-protein interaction mechanism, we performed an analysis of amino acid sequences using ProtParam software (*33*), which indicated a net positive charge of +8 for ferricyt c. Hence, an electrostatic attraction should occur between Fe_3O_4-NPs and protein molecules, resulting in physisorption processes. Indeed, while the zeta potential for Fe_3O_4-NPs indicates a highly negatively charged surface at pH 7.4 (Fig. 2G, blue), ferricyt c is positively charged (7.5 ± 0.6 mV) (Fig. 2G, red). For Fe_3O_4-NPs-Cyt c suspension, the zeta potential has an intermediate value (-26.2 ± 0.4 mV) (Fig. 2G, black), suggesting that some of the surface charges were compensated by mutual attraction. The Fe_3O_4-NPs-Cyt c interaction is also evidenced by the hydrodynamic diameters from dynamic light scattering (DLS), where the three size distributions correspond to nonadsorbed protein molecules (3 ± 2 nm), free Fe_3O_4-NPs (19 ± 2 nm) and a Fe_3O_4-

NPs-cyt c system at 51 ± 2 nm (Fig. 2H). The physisorption process was studied with UV-vis spectroscopy to monitor changes in aqueous ferricyt c concentration. Within the first 10 min, approximately 34% of the protein molecules were adsorbed by the nanoparticles (Fig. S4). The potential map for ferricyt c in Fig. 2I suggests that electrostatic forces govern the interaction between the NPs and the protein heme moiety since its charge distribution is inhomogeneous around the heme group. This effect induces a favorable electrostatic interaction between Fe_3O_4-NPs and ferricyt c under neutral conditions.

The interaction mechanism was further studied through the fluorescence quenching effect. When ferricyt c is excited at 300 nm, the emission spectrum displays a strong band at 346 nm assigned to its single tryptophan (Trp) amino acid residue (*34*). Upon the addition of increasing concentrations of Fe_3O_4-NPs, there is a progressive reduction in the maximum protein fluorescence (Fig. S5). The nature of the quenching mechanism was determined with experiments at 15, 25, and 35 ºC to calculate the Stern-Volmer constant (K_{sv}) (Fig. S6). The plots are linear for low Fe_3O_4-NPs concentrations, but they depart upward significantly at high concentrations. This effect supports the hypothesis of a combined dynamic and static quenching at higher NPs concentrations, while a single dynamic quenching would prevail at lower NPs concentrations (*34*). The K_{sv} values in Table S2 obtained with the linear portion of the Stern-Volmer plots in Fig. S6A show a direct correlation between the rise in temperature and NPs concentration. The bimolecular quenching constant (K_q) calculation reinforces the hypothesis that a percentage of the quencher interacts with the fluorophore through a static quenching since purely dynamic processes generally exhibit K_q maximum values around 10^{10} L $mol^{-1}s^{-1}$; however, for Fe_3O_4-NPs-Cyt c interactions K_q is ca. 10^{11} L mol^{-1} s^{-1} (Table S2). In other words, a complex is formed between Fe_3O_4-NPs and ferricyt c, which corroborates the physisorption result. With an increase in temperature, the number of binding sites per protein molecule (n) and the binding constant (K_b) increase (Table 2), since heating leads to tertiary conformational changes in the protein, favoring NP-protein binding.

An associative mechanism in the transition state with an enthalpy-driven process

The kinetic characterization of ferricytochrome c reduction by Fe_3O_4-NPs was investigated using *in situ* UV-vis absorption spectroscopy with the experiments carried out in a pseudo-first-order regime. Although the NPs were at least ten times more concentrated than the protein, the extent of its reduction was incomplete in all experiments. The most plausible reason for this finding

is that the reaction equilibrium is reached before all the ferricytochrome c reacts as the redox potential difference between the Fe_3O_4-NPs and protein decreases to zero. Fig. S7A depicts the dependence of ferrouscytochrome c formation with time from monitoring the maximum absorbance at 550 nm at 25, 30, 35, and 40 ºC. The apparent pseudo-first-order rate constant (k_{obs}) and the second-order rate constant (k) at various T were calculated (see Fig. S7B and 3A, respectively), where k increases with T, with $k = 2.63 \pm 0.05$ L mol^{-1} s^{-1} at 25 ºC. As shown in Fig. S8 and S9, once in its reduced state the protein tends to re-oxidize under O_2 atmosphere, but with a k_{obs} ten thousand times slower ($k_{obs} = 9.72 \times 10^{-7}$ s^{-1}) than k_{obs} for its reduction by Fe_3O_4-NPs ($k_{obs} = 1.74 \times 10^{-3}$ s^{-1}), indicating that this re-oxidation is kinetically unfavorable.

Using these results and the Arrhenius equation, we calculated the protein reduction activation energy (E_a), which is 40.2 ± 1.5 kJ mol^{-1} (Fig. 3B). Detailed information on the reaction mechanism was obtained by calculating the activation parameters (Fig. S10) (*35*), including enthalpy of activation ($\Delta H^{\ddagger} = +37.9 \pm 1.5$ kJ mol^{-1}) and entropy of activation ($\Delta S^{\ddagger} = -109 \pm 6.34$ J mol^{-1} K^{-1}). Near room temperature, E_a is ca. 2.5 kJ mol^{-1} larger than $\Delta H^{\ddagger}$, which was close to what we have observed. $\Delta S^{\ddagger}$ is particularly large and negative, as is often the case for a second-order reaction via a bimolecular step. The entropy decrease is related to the associative mechanism with the two reactants species converging into a single transition state (*36*). Thermodynamic parameters such as free energy of binding ($\Delta G^{o}_{binding}$), enthalpy (ΔH^{o}), and entropy (ΔS^{o}) were estimated using the fluorescence measurements (Table S3). During the binding of NPs to the protein, there is a displacement of associated water molecules, which reflects in a positive ΔS^{o} change of the entire system (*37*). Although our system is enthalpy driven – since the magnitude of ΔH^{o} out-weighs those of ΔS^{o} – this is an indication of both electrostatic and hydrophobic/hydrogen bonds interactions between the species (*38*). As shown in Table S3, $\Delta G^{o}_{binding}$ values are negative; i.e., it is a spontaneous process. Fig. 3C illustrates the ferricytochrome c reduction by Fe_3O_4-NPs, which requires a $\Delta G^{\ddagger}$ of + 70.4 kJ mol^{-1} and an overall ΔG^{o} of -273.6 kJ mol^{-1} involving the binding energy between the protein and the NPs, in addition to the electron transfer reaction itself. Therefore, the Fe_3O_4-NPs interact with ferricytochrome c inducing a spontaneous ET, with contributions of electrostatic binding and van der Waals/hydrogen bonds. Interestingly, this mechanism is similar to that in the mitochondrial respiratory chain between complex III and Cyt c (*39*).

γ-Fe_2O_3-NPs as a biomimetic complex IV

The intrinsic peroxidase-like activity of Fe_3O_4-NPs is well known (*40*), with Fe^{2+} ions in their crystalline structure playing a dominant role in their activity. Hence, the enzyme mimetic activity from the nanoparticles should increase with the proportion of Fe^{2+} ions. We performed experiments with bare γ-Fe_2O_3-NPs (Fig. S11) (*41*) to investigate the roles of Fe^{2+} and Fe^{3+} ions in the redox activity. Fig. 3D shows two sets of measurements under the same experimental conditions, with Fe_3O_4-NPs (red line) and γ-Fe_2O_3-NPs (green line) in the presence of ferricytochrome c. Ferricytochrome c was reduced while reacting with Fe_3O_4-NPs. In contrast, γ-Fe_2O_3-NPs do not exhibit reducing activity towards the protein (that remained oxidized), as indicated by the Q bands spectra at 0 min (black line) and 15 min (red line) after contact between the species (Fig. S12). Therefore, the redox activity of bare Fe_3O_4-NPs requires Fe^{2+} ions on their surface, being oxidized by ferricytochrome c to generate a new Fe^{3+}-enriched surface.

As previously mentioned, a different redox behavior was observed with γ-Fe_2O_3-NPs. After approximately 30 min in the presence of these NPs, most of ferrouscytochrome c was oxidized to ferricytochrome c with $k_{obs} = 1.1 \times 10^{-4}$ s^{-1} (Fig. S13). This behavior was shown by a progressive disappearance of the absorption bands at 520 and 550 nm (blue lines), in addition to a small, single band at 530 nm (red lines) (Fig. 3E) and a progressive appearance of a band at 700 nm assigned to the Fe-S(Met) bond (see Fig. S14). In this case, an increase in superficial Fe^{2+} concentration on γ-Fe_2O_3-NPs should be expected after oxidation of ferrouscytochrome c, which is the opposite behavior from the protein reduction by Fe_3O_4-NPs. Therefore, we can also infer that γ-Fe_2O_3-NPs behave as a biomimetic material for complex IV from the mitochondrial respiratory chain.

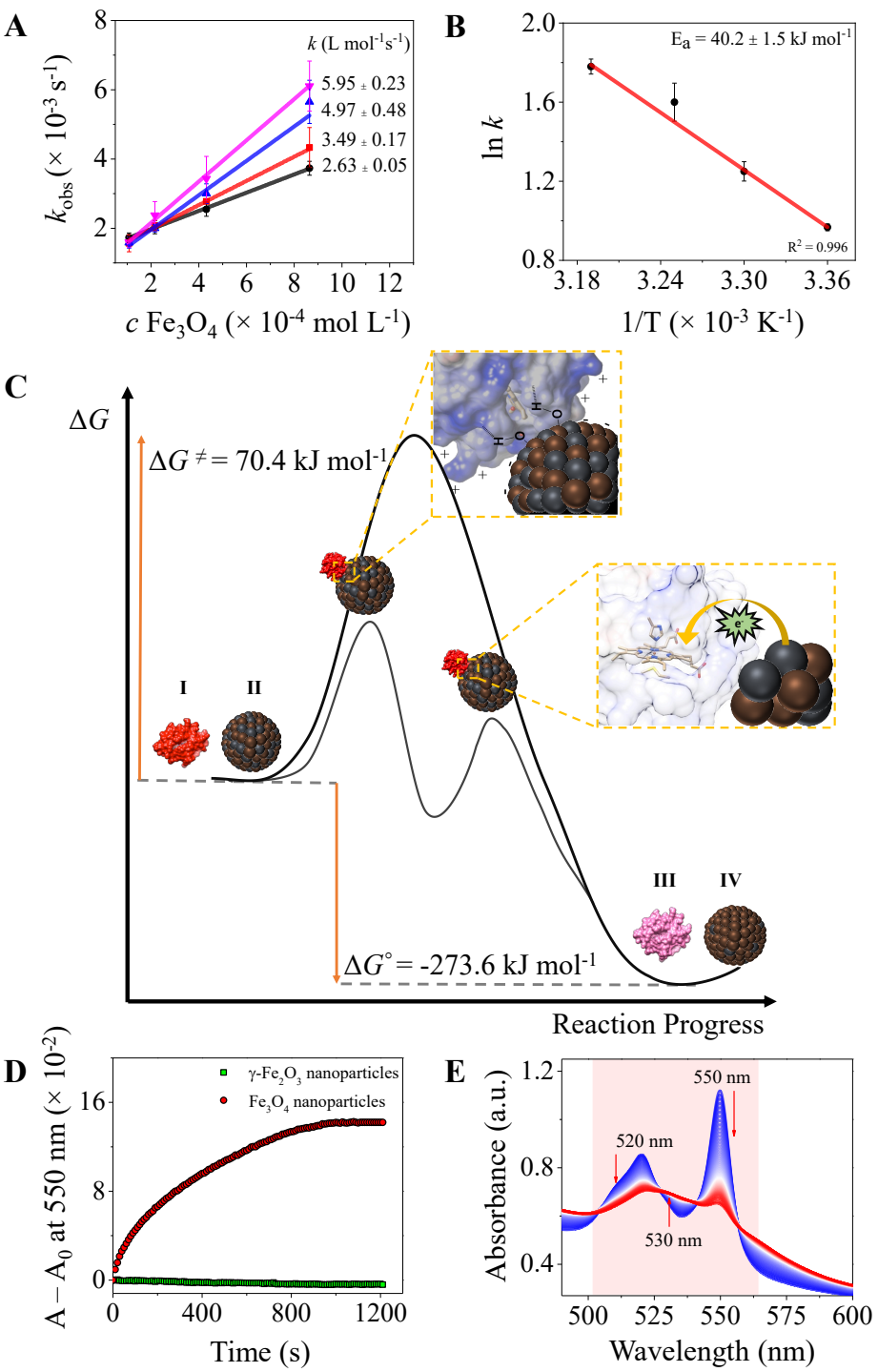

Fig. 3. (**A**) Dependence of k_{obs} on the concentration of Fe_3O_4-NPs for various T: 25 (●), 30 (●), 35 (●) and 40 ºC (●). Also indicated is k calculated for each T; (**B**) E_a from the Arrhenius plot; (**C**) Schematic representation of ferricyt c (**I**) reduction by Fe_3O_4-NPs (**II**), with $\Delta G^{\ddagger}$ and $\Delta G^{\circ}_{binding}$ energies. $\Delta G^{\ddagger}$ requires Coulombic and van der Waals interactions between the species, followed by ET from the NP Fe^{2+} sites to the protein heme group, resulting in ferrouscyt c (**III**) and a partially oxidized NP (**IV**); (**D**) Comparison between the redox activity of γ-Fe_2O_3-NPs and Fe_3O_4-NPs towards ferricyt c; (**E**) Ferrouscyt c oxidation by γ-Fe_2O_3-NPs throughout the time indicated by the fading of the bands at 520 and 550 nm and the appearance of one single band at 530 nm.

NPs redox activity behavior incorporated in a mitochondrial cell membrane model

In order to mimic the catalytic step that shows the redox activity of complex III and IV towards Cyt c, Fe_2O_3-NPs and γ-Fe_2O_3-NPs were incorporated in a Langmuir-Blodgett (LB) film

employed as a simplified mitochondrial cell membrane model (see Fig. 1 and 4A). The LB film was transferred from a Langmuir monolayer made with a mixture of lipids representing the classes most frequent in eukaryotic cells, viz. phosphatidylcholines (PC), phosphatidylethanolamines (PE), and cardiolipin (CL) (*42*). Fig. S15 shows the surface π-*A* isotherms for 1,2-dipalmitoyl-sn-glycero-3-phosphocholine (DPPC, black), 1,2-dipalmitoyl-sn-glycero-3-phosphoethanolamine (DPPE, red), 1,1',2,2'-tetramyristoyl cardiolipin (CL, blue), and DPPC-DPPE-CL (pink) corresponding to the model membrane composition.

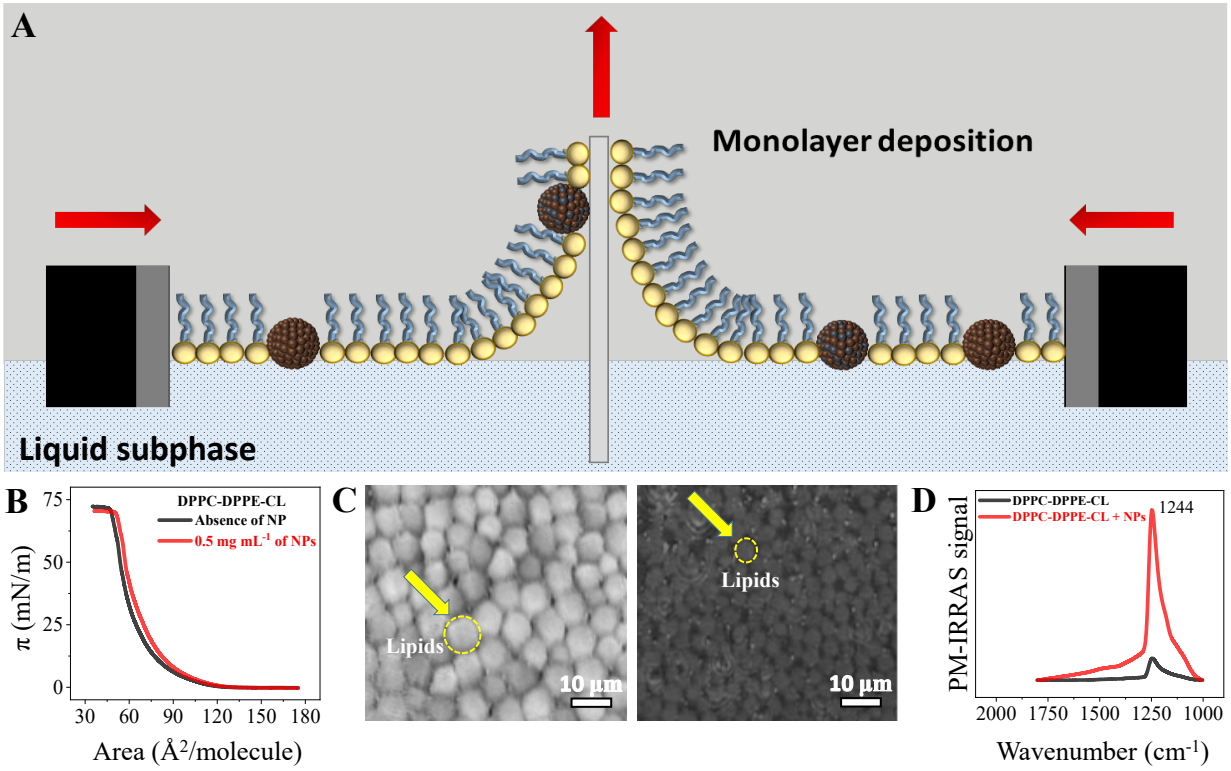

Fig. 4. Mitochondrial cell membrane model characterization. (**A**) Langmuir-Blodgett monolayer fabrication: the ternary lipid mixture in the presence of NPs is spread over the subphase surface and then compressed with two symmetric moving barriers to be transferred onto the supporting glass; (**B**) DPPC-DPPE-CL monolayers in the absence (●) and in presence (●) of a Fe_3O_4-NPs/γ-Fe_2O_3-NPs mixture. It should be noted that the sizes of molecules and nanoparticles are not in the same scale; (**C**) Zoomed BAM images of DPPC-DPPE-CL collected on PBS subphase without (left side) and with (right side) a 0.05 mg mL^{-1} mixture of Fe_3O_4-NPs/γ-Fe_2O_3-NPs, respectively, at 30 mN m^{-1} of the monolayer compression. (**D**) PM-IRRAS spectra of LB films made of DPPC-DPPE-CL (●) and DPPC-DPPE-CL + a mixture of Fe_3O_4-NPs/γ-Fe_2O_3-NPs (●) in the polar region;

The isotherm for the Langmuir monolayer of DPPC-DPPE-CL is slightly expanded by the incorporation of a mixture of Fe_3O_4-NPs/γ-Fe_2O_3-NPs into the lipid chains (Fig. 4B). Such

incorporation was confirmed by Brewster angle microscopy (BAM) images taken at four stages: at 0 mN m^{-1} (with no compression), at 18 mN m^{-1} (in the liquid-expanded phase), at 30 mN m^{-1} (corresponding to the lateral pressure of natural cell membranes), and at 60 mN m^{-1} (after monolayer collapse). Fig. S16 shows these images and zoomed pictures are shown in Fig. 4C. In the absence of NPs, the DPPC-DPPE-CL monolayer at 30 mN m^{-1} is compact and homogeneous; however, when NPs are present, this homogeneity vanishes. As the nanoparticle-containing monolayers are transferred onto solid supports in the form of LB films, a larger effect is observed according to polarization-modulation infrared reflection absorption spectroscopy (PM-IRRAS) data. Fig. 4D shows a sharp increase in intensity for the band at 1244 cm^{-1} assigned to PO_2^- asymmetric stretching (*43*) in the polar region. Other bands related to the polar groups are affected, as seen in Fig. S17. Furthermore, the spectra for the hydrophobic region in Fig. S18 indicate changes in the bands assigned to CH_2 and CH_3 stretching when comparing LB films with or without the mixture of Fe_3O_4-NPs/γ-Fe_2O_3-NPs. Hence, the interaction of NPs with polar heads and alkyl chains affects the organization and ordering of the lipids in the model membrane, consistent with the loss of homogeneity observed in the BAM images.

The LB films were used to demonstrate the biomimetic activity of NPs as non-proteinaceous mimetic of complexes III and IV responsible for ET in the final steps of the mitochondrial respiratory chain. Electrochemical assays show no redox processes either for DPPC-DPPE-CL LB film (Fig. 5A, black) or for the DPPC-DPPE-CL LB film in the presence of ferricytochrome c (Fig. 5A, red). For the latter, there is an ohmic drop since the lipid membrane partially blocks the ET between the electrode and protein. In contrast, for the LB films containing the NPs, Fig. 5A shows a well-defined quasi-reversible redox couple ($E^{0'}$ = 57.5 mV *vs* $Ag/AgCl_{sat}$) in the presence of ferricytochrome c. This redox couple is related to Fe^{3+}/Fe^{2+} of the heme group (*44*), indicating indeed that ET occurs across the lipid membrane with the aid of incorporated NPs. Additionally, results with *in situ* electron spectroscopy with the experimental set-up illustrated in Fig. 5B showed no redox activity for DPPC-DPPE-CL LB film towards the protein (Fig. 5C, black and red lines). However, within a few minutes, a reduction of ferricytochrome c occurs for the DPPC-DPPE-CL-NPs LB film, as seen in Fig. 5D with the expected split in the Q band.

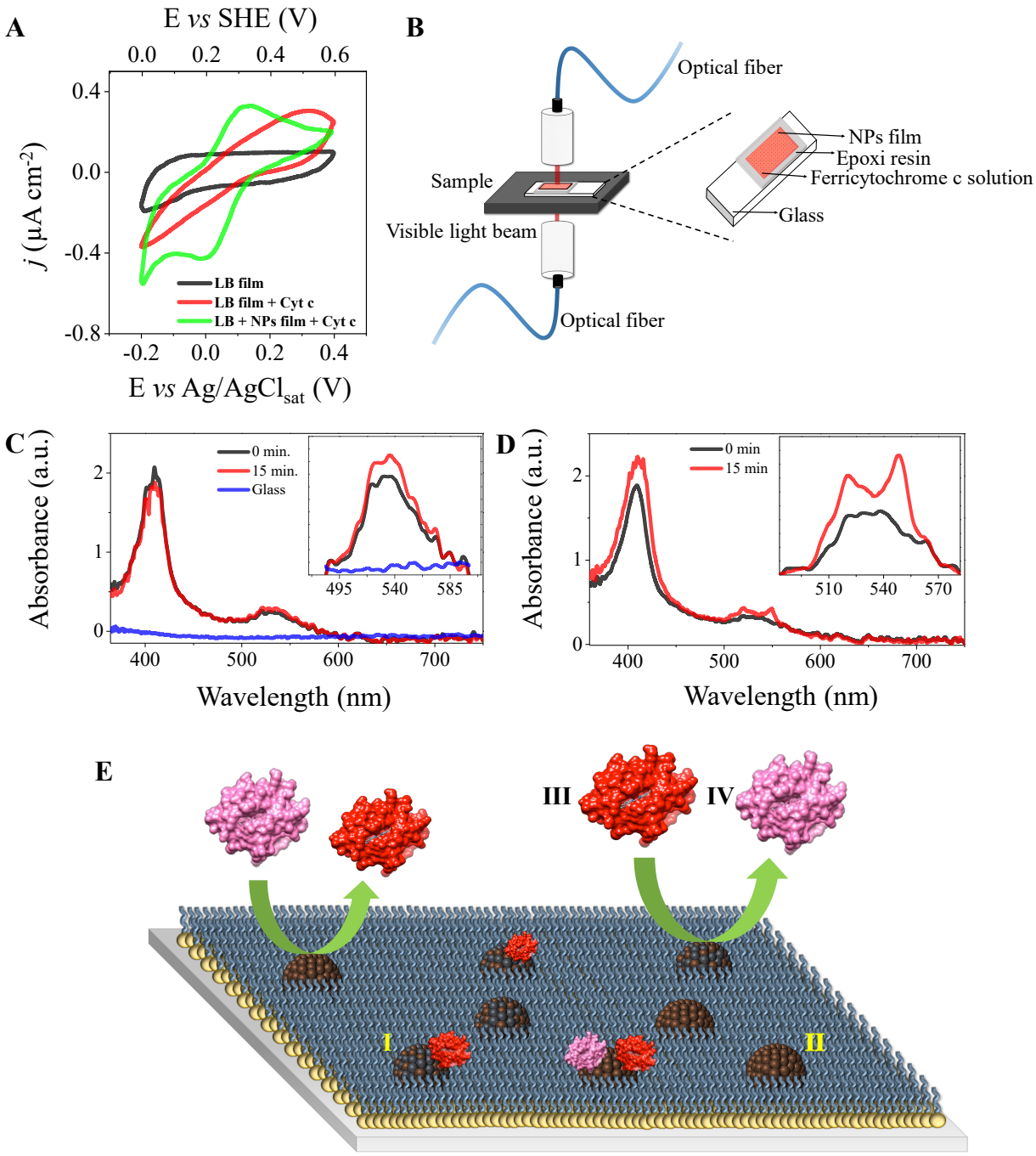

Fig. 5. ET across the lipid membrane. (**A**) CV curves for LB film (●), LB film + Cyt c (●) and LB + NPs film + Cyt c (●) (Scan rate: 5 mV s^{-1} at 25ºC); (**B**) Experimental set-up for *in situ* electronic spectroscopy; (**C**) Electronic absorption spectra of the supporting glass (●) and LB film + ferricyt c at 0 min (●) and after 15 min (●). The insert shows the Q band expanded region; (**D**) Electronic absorption spectra of LB + NPs film + ferricyt c at 0 min (●) and after 15 min (●). The insert shows the Q band expanded region; (**E**) Representation of the biomimetic membrane with the Fe_3O_4-NPs (**I**) and γ-Fe_2O_3-NPs (**II**) mimicking the complexes III and IV of the respiratory chain, respectively. Ferricytochrome c is in red (**III**) while ferrouscytochrome c is in pink (**IV**).

Fig. 5E illustrates the process on a nanoscopic-mesoscopic scale. As soon as the protein is added to the system, electrostatic and non-polar interactions arise. Some of the protein molecules are adsorbed onto the NPs while others just collide onto them, leading to ET processes. As the ferricytochrome c molecules interact with Fe_3O_4-NPs, the content of superficial Fe^{2+} of NPs decrease and the protein reduces. This generates ferrouscytochrome c that interacts with γ-Fe_2O_3-NPs, leading to the opposite reaction, i.e., increasing the nanoparticle superficial Fe^{2+} content and oxidizing the protein. This process continues until the system reaches the equilibrium at 15 min. Then, no apparent changes in the system composition occur due to the possible presence of a protective layer of Cyt c covering the NPs surface, which causes a steric hindrance to the surface access by new protein molecules.

CONCLUSIONS

We presented a molecular-level mechanistic insight of the heterogeneous electron transfer ET between nanosized iron oxides and Cyt c, in addition to the design of a bioinspired system for the mitochondrial respiratory chain. We observed direct ET between crystalline Fe_3O_4-NPs and γ-Fe_2O_3-NPs and the protein, without significant changes in its secondary and tertiary structure. The protein-nanoparticles interactions are mainly electrostatic and non-polar forces involving the heme moiety, similarly to what is observed for soluble Cyt c and the complexes III and IV in the respiratory chain. Kinetic and thermodynamic parameters indicated an associative mechanism in the transition state and an enthalpy-driven spontaneous reaction for the ferricytochrome c reduction. The extent of the reaction depends on the Fe^{2+}/Fe^{3+} ratio on the surface of the nanoparticles, since superficial Fe^{2+} ions control ferricytochrome c reduction while ferrouscytochrome c oxidation depends on superficial Fe^{3+} ions. Finally, when incorporated in a lipid membrane cell model, Fe_3O_4-NPs and γ-Fe_2O_3-NPs maintain their redox activity, catalyzing ET similarly to complexes III and IV of the mitochondrial respiratory chain, respectively, i.e., mimicking their activity.

ACKNOWLEDGMENTS

Funding: This work was supported by the National Council for Scientific and Technological Development – CNPq (I. A. M. process 134396/2018-9), Coordinating Agency for Advanced

Training of Graduate Personnel (CAPES) and São Paulo Research Foundation – FAPESP (L. J. A. M. process 2017/20493-2, A. R. P. process 2018/00878-0, O.N.O. processes 2017/03879-4 and F. N. C. processes 2019/15333-1 and 2019/12053-8). **Author contributions:** I. A. M., A. F. A. A. M., and F. N. C. conceived the project. F. N. C. and O. N. O. supervised the project. I. A. M. prepared, conceived and carried out the NPs characterization experiments, zeta potential, DLS, UV-vis, CD and fluorescence experiments. I. A. M. and L. J. A. M. conducted the FTIR and electrochemical experiments. I. A. M. and A. R. P. conducted the experiments with the mitochondrial membrane model. This manuscript was written and revised through contribution of all authors. **Competing interests:** Authors declare no competing interests; **Data and materials availability:** All data is available in the main text or the supplementary materials.

REFERENCES

1. Kumar, L. H. H. Hsu, P. Kavanagh, F. Barrière, P. N. L. Lens, L. Lapinsonnière, J. H. Lienhard, U. Schröder, X. Jiang, D. Leech, The ins and outs of microorganism-electrode electron transfer reactions. *Nat. Rev. Chem.* **1**, 1–13 (2017).
2. H. Gong, J. Li, A. Xu, Y. Tang, W. Ji, R. Gao, S. Wang, L. Yu, C. Tian, J. Li, H. Y. Yen, S. M. Lam, G. Shui, X. Yang, Y. Sun, X. Li, M. Jia, C. Yang, B. Jiang, Z. Lou, C. V. Robinson, L. L. Wong, L. W. Guddat, F. Sun, Q. Wang, Z. Rao, An electron transfer path connects subunits of a mycobacterial respiratory supercomplex. *Science* **362**, 1-11 (2018).
3. J. Liu, S. Chakraborty, P. Hosseinzadeh, Y. Yu, S. Tian, I. Petrik, A. Bhagi, Y. Lu, Metalloproteins containing cytochrome, iron-sulfur, or copper redox centers. *Chem. Rev.* **114**, 4366–4369 (2014).
4. X. Wang, R. Clément, M. Roger, M. Bauzan, I. Mazurenko, A. de Poulpiquet, M. Ilbert, E. Lojou, Bacterial Respiratory Chain Diversity Reveals a Cytochrome c Oxidase Reducing O 2 at Low Overpotentials . *J. Am. Chem. Soc.* **141**, 11093–11102 (2019).
5. V. Balasubramanian, A. Correia, H. Zhang, F. Fontana, E. Mäkilä, J. Salonen, J. Hirvonen, H. A. Santos, Biomimetic Engineering Using Cancer Cell Membranes for Designing Compartmentalized Nanoreactors with Organelle-Like Functions. *Adv. Mater.* **29**, 1–7 (2017).
6. V. Balasubramanian, A. Poillucci, A. Correia, H. Zhang, C. Celia, H. A. Santos, Cell Membrane-Based Nanoreactor to Mimic the Bio-Compartmentalization Strategy of a Cell. *ACS Biomater. Sci. Eng.* **4**, 1471–1478 (2018).
7. L. Otrin, N. Marušič, C. Bednarz, T. Vidaković-Koch, I. Lieberwirth, K. Landfester, K. Sundmacher, Toward Artificial Mitochondrion: Mimicking Oxidative Phosphorylation in Polymer and Hybrid Membranes. *Nano Lett.* **17**, 6816–6821 (2017).
8. A. Byrne, J. M.; Klueglein, N.; Pearce, C.; Rosso, K. M.; Appel, E.; Kappler, Redox cycling of Fe(II) and Fe(III) in magnetite by Fe-metabolizing bacteria. *Science* **347**, 1473–1476 (2015).
9. E. D. Melton, E. D. Swanner, S. Behrens, C. Schmidt, A. Kappler, The interplay of

microbially mediated and abiotic reactions in the biogeochemical Fe cycle. *Nat. Rev. Microbiol.* **12**, 797–808 (2014).
10. M. F. Hochella, S. K. Lower, P. A. Maurice, R. L. Penn, N. Sahai, D. L. Sparks, B. S. Twining, Nanominerals, mineral nanoparticles, and earth systems. *Science.* **319**, 1631–1635 (2008).
11. M. F. Hochella, D. W. Mogk, J. Ranville, I. C. Allen, G. W. Luther, L. C. Marr, B. P. McGrail, M. Murayama, N. P. Qafoku, K. M. Rosso, N. Sahai, P. A. Schroeder, P. Vikesland, P. Westerhoff, Y. Yang, Natural, incidental, and engineered nanomaterials and their impacts on the Earth system. *Science* **363**, 1-10 (2019).
12. M. Liang, X. Yan, Nanozymes: From New Concepts, Mechanisms, and Standards to Applications. *Acc. Chem. Res.* **52**, 2190–2200 (2019).
13. A. F. A. A. Melo, G. C. Sedenho, I. Osica, K. Ariga, F. N. Crespilho, Electrochemical behavior of cytochrome c immobilized in a magnetically induced mesoporous framework. *ChemElectroChem.* **6**, 5802-5809 (2019).
14. H. Xu, J. Chang, H. Wang, Y. Liu, X. Zhang, P. Liang, X. Huang, Enhancing direct interspecies electron transfer in syntrophic-methanogenic associations with (semi)conductive iron oxides: Effects and mechanisms. *Sci. Total Environ.* **695**, 133876 (2019).
15. F. Yazdani, M. Seddigh, Magnetite nanoparticles synthesized by co-precipitation method: the effects of various iron anions on specifications. *Mater. Chem. Phys.* **184**, 318-323 (2016).
16. U. Holzwarth, N. Gibson. The Scherrer equation versus the "Debye-Scherrer quation". *Nat. Nanotechnol.* **6**, 534 (2011).
17. H. Yang, S. Yang, J. Kong, A. Dong, S. Yu, Obtaining information about protein secondary structures in aqueous solution using Fourier transform IR spectroscopy. *Nat. Protoc.* **10**, 382–396 (2015).
18. A. Johs, L. Shi, T. Droubay, J. F. Ankner, L. Liang, Characterization of the Decaheme c-type cytochrome OmcA in solution and on hematite surfaces by small angle X-ray scattering and neutron reflectometry. *Biophys. J.* **98**, 3035-3043 (2010).
19. Lakowicz, J. R. Quenching of Fluorescence *In:* Principles of Fluorescence Spectroscopy, 3ª ed., Springer, USA, 2006.
20. J. S. Zhou, E. S. V. Granada, N. B. Leontis, M. A. J. Rodgers. Photoinduced electron transfer in self-associated complexes of several uroporphyrins and cytochrome c. *J. Am. Chem. Soc.* **112**, 5074-5080 (1990)
21. M. Vincent, J. C. Brochon, F. Merola, W. Jordi, J. Gallay. Nanosecond dynamics of horse heart apocytochrome c in aqueous solution as studied by time-resolved fluorescence of the single tryptophan residue (Trp-59). *Biochem.* **27**, 8752-8761 (1988).
22. Laidler, K. J. *Chemical Kinetics*, 3rd ed., Pearson Education Inc., USA, 1987.
23. M. Menzinger, R. Wolfgang, The Meaning and Use of the Arrhenius Activation Energy. *Angew. Chemie Int. Ed. English*. **8**, 438–444 (1969).
24. Y. Hu, Y. Liu, X. Shen, X. Fang, S. Qu. Studies on the interaction between 1-hexylcarbamoyl-5-fluorouracil and bovine serum albumin. *J. Mol. Struct.* **738**, 143-147 (2005).
25. I. Nurdin, M. R. Johan, I. I. Yaacob, B. C. Ang, Effect of nitric acid concentrations on synthesis and stability of maghemite nanoparticles suspension. *Sci. World J.* **2014**, Article ID 589479 (2014).

26. G. P. Santos, A. F. A. A. Melo, F. N. Crespilho, Magnetically controlled single-nanoparticle detection via particle-electrode collisions. *Phys. Chem. Chem. Phys.* **16**, 8012–8018 (2014).
27. A. F. A. A. Melo, A. Hassan, L. J. A. Macedo, I. Osica, L. K. Shrestha, Q. Ji, O. N. Oliveira Jr., J. Henzie, K. Ariga, F. N. Crespilho, Microwires of Au-Ag nanocages patterned via magnetic nanoadhesives for investigating proteins using surface enhanced infrared absorption spectroscopy. *ACS Appl. Mater. Interfaces* **11**, 18053-18061 (2019).
28. J. M. Antosiewicz, D. Shugar, UV--Vis spectroscopy of tyrosine side-groups in studies of protein structure. Part 2: selected applications. *Biophys. Rev.* **8**, 163–177 (2016).
29. H. Z. Zhao, Q. Du, Z. S. Li, Q. Z. Yang, Mechanisms for the direct electron transfer of cytochrome c induced by multi-walled carbon nanotubes. *Sensors (Switzerland)*. **12**, 10450–10462 (2012).
30. M. W. Mara, R. G. Hadt, M. E. Reinhard, T. Kroll, H. Lim, R. W. Hartsock, R. Alonso-Mori, M. Chollet, J. M. Glownia, S. Nelson, D. Sokaras, K. Kunnus, K. O. Hodgson, B. Hedman, U. Bergmann, K. J. Gaffney, E. I. Solomon, Metalloprotein entatic control of ligand-metal bonds quantified by ultrafast x-ray spectroscopy. *Science* **356**, 1276–1280 (2017).
31. J. Liu, C. I. Pearce, C. Liu, Z. Wang, L. Shi, E. Arenholz, K. M. Rosso, Fe 3-x Ti x O 4 nanoparticles as tunable probes of microbial metal oxidation. *J. Am. Chem. Soc.* **135**, 8896–8907 (2013).
32. S. M. Kelly, T. J. Jess, N. C. Price, How to study proteins by circular dichroism. *Biochim. Biophys. Acta - Proteins Proteomics*. **1751**, 119–139 (2005).
33. E. Gasteiger, C. Hoogland, A. Gattiker, S. Duvaud, M. R. Wilkins, R. D. Appel, A. Bairoch, in *The Proteomics Protocols Handbook*, J. M. Walker, Ed. Humana Press, New York, USA, 2005.
34. Lakowicz, J. R. Quenching of Fluorescence *In:* Principles of Fluorescence Spectroscopy, 3ª ed., Springer, USA, 2006.
35. D. A. Pixton, C. A. Petersen, A. Franke, R. Van Eldik, E. M. Garton, C. R. Andrew, Activation parameters for heme-NO binding in alcaligenes xylosoxidans cytochrome c': The putative dinitrosyl intermediate forms via a dissociative mechanism. *J. Am. Chem. Soc.* **131**, 4846–4853 (2009).
36. Laidler, K. J. Chemical Kinetics, 3ª ed., Pearson, USA, 1987.
37. X. Du, Y. Li, Y. Xia, S. Ai, J. Liang, P. Sang, X. Ji, S. Liu, Insights into protein-ligand interactions: mechanisms, models, and methods. *Int. J. Mol. Sci.* **17**, 144 (2016).
38. J. Yu, L. Yang, X. Liang, T. Dong, H. Liu, Bare magnetic nanoparticles as fluorescence quenchers for detection of thrombin. *Analyst*. **140**, 4114–4120 (2015).
39. S. R. N. Solmaz, C. Hunte, Structure of complex III with bound cytochrome C in reduced state and definition of a minimal core interface for electron transfer. *J. Biol. Chem.* **283**, 17542–17549 (2008).
40. L. Gao, J. Zhuang, L. Nie, J. Zhang, Y. Zhang, N. Gu, T. Wang, J. Feng, D. Yang, S. Perrett, X. Yan, Intrinsic peroxidase-like activity of ferromagnetic nanoparticles. *Nat. Nanotechnol.* **2**, 577 (2007).
41. I. Nurdin, M. R. Johan, I. I. Yaacob, B. C. Ang, Effect of nitric acid concentrations on synthesis and stability of maghemite nanoparticles suspension. *Sci. World J.* **2014**, Article ID 589479 (2014).
42. S. E. Horvath, G. Daum, Lipids of mitochondria. *Prog. Lipid Res.* **52**, 590–614 (2013).

43. R. Mendelsohn, G. Mao, C. R. Flach, Infrared reflection-absorption spectroscopy: Principles and applications to lipid-protein interaction in Langmuir films. *Biochim. Biophys. Acta - Biomembr.* **1798**, 788–800 (2010).
44. R. A. S. Luz, F. N. Crespilho, Gold nanoparticle-mediated electron transfer of cytochrome c on a self-assembled surface. *RSC Adv.* **6**, 62585–62593 (2016).